Three-Dimensional Interactions in the Rotor of an Axial Turbine

H. P. Hodson* and M. R. Banieghbal†
University of Cambridge, Cambridge CB3 ODY, England, United Kingdom
and
G. M. Dailey‡
Rolls–Royce plc, Derby DE2 8BJ, England, United Kingdom

This article presents a study of the development of the three-dimensional flowfield within the rotor blades of a low-speed, large-scale axial flow turbine. Measurements have been performed in the rotating and stationary frames of reference. Time-mean data have been obtained using miniature five-hole pneumatic probes, whereas the unsteady development of the flow has been determined using three-axis subminiature hot-wire anemometers. Additional information is provided by the results of blade-surface flow-visualization experiments and surface-mounted hot-film anemometers. The development of the stator exit flow, as it passes through the rotor blades, is described. Unsteady data suggest that the presence of the rotor secondary and tip leakage flows restricts the region of unsteady interaction to near midspan when the stator wakes and secondary flows are adjacent to the suction surface. Surface-mounted hot-film data show that this affects the suction-side laminar-turbulent transition process.

Nomenclature

C_x	= axial chord
E	= anemometer voltage
E_0	= anemometer voltage under zero-flow conditions
H	= boundary-layer shape factor δ^*/θ
P_0	= stagnation pressure
Re	= Reynolds number
s	= surface distance
s^*	= fractional surface distance, s/s_{max}
$T_{u_{rms}}$	= intensity of random velocity fluctuations, rms/V_{ref}
t	= time measured from once-per-revolution trigger
t^*	= fractional time, t/τ
U_m	= mean blade velocity
V	= velocity
V_{ref}	= stator midspan mean exit velocity
δ^*	= boundary-layer displacement thickness
θ	= boundary-layer momentum thickness
ρ	= density
τ	= periodic time
τ_w	= wall shear stress, $(E^2/E_0^2 - 1)^3$, arbitrary units
ω	= stagnation pressure loss coefficient, $\Delta P_0/\frac{1}{2}\rho V_{ref}^2$
$-$	= time-mean
$\langle\langle\ \rangle\rangle$	= ensemble-variance of . . .
$\langle\ \rangle$	= ensemble-mean of . . .

Introduction

T HE need for a better understanding of the effects of periodic blade row interactions on the aerodynamic and thermodynamic performance of axial turbines is ever increasing. The periodic flow occurs as a result of the relative motion of adjacent blade rows and gives rise to several types of interaction.

Wakes[1] and secondary flow (including tip leakage) vortices[2,3] from an upstream blade row give rise to periodic fluctuations of the mean flow and turbulence at inlet to the following blade row.

The interactions of wakes with succeeding blade rows have received much attention in recent years. The interactions have been studied using turbomachines[4] and simulations.[5] Much of this research has concluded that the most significant effect is the periodic forcing of the transition of the blade surface boundary layers and the influence this has upon the aerodynamic and thermodynamic performance of the blade row.[6,7] It has also been shown that as an upstream wake convects through the blade passage, it is cut, stretched, and sheared as a consequence of the differing convection rates across the blade passage.[1,5] In addition, the velocity defect within the wake causes a transport of wake fluid across the blade passage toward the suction side during its passage through the blade row as the wake behaves like a "negative-jet".[1] However, the effect of the negative-jet appears to be less significant than either the effects of bulk convection or the effects of turbulence within the wakes.

In low-aspect-ratio turbines, the blade row interactions may be dominated by the effects of incoming secondary flow vortices rather than by the wakes. For example, it is possible for the incoming vortices to burst,[8] giving rise to very high levels of freestream turbulence. In highly loaded stages,[2,9] it has been observed that the interaction of the secondary flows with the succeeding blade row appears to dominate the flowfield, even at the exit from the succeeding blade row. Nevertheless, descriptions of the convection of the secondary flow vortices through the blade passage are similar to those of the convection of wakes. Hence, it might be concluded that the incoming vortices are chopped, stretched, bowed, and sheared in similar ways to the wakes. Stretching a vortex will tend to increase its secondary kinetic energy. This may explain the dominant effect of the secondary flow vortices on the unsteady flowfield in highly loaded low aspect ratio machines. Although less significant, similar interactions have been observed in low-pressure turbines[10,11] and less highly loaded high-pressure turbine blade rows.[3]

*Lecturer, Whittle Laboratory, Madingley Road. Member AIAA.
†Research Associate, Whittle Laboratory, Madingley Road.
‡Research Engineer, P.O. Box 31.

The potential influence of a blade extends both upstream and downstream, and decays exponentially with a length scale typically of the order of the chord or pitch. In axial turbines, the blade row spacings are typically of the order of one-quarter to one-half of a blade chord. When this spacing is near the lower limit, potential and viscous flow interactions may co-exist.[12] In transonic stages, interactions may also arise as the direct result of the impingement of the trailing shock waves upon the downstream blade row.[5] However, it is likely that in many cases the effect of the viscous flow interactions will dominate the development of the unsteady flow in the downstream blade row.

This article is specifically concerned with the interactions of incoming viscous flow features such as wakes and secondary flow vortices. The development of the flow in the rotor passage of an axial turbine stage is described. Given that much of the loss on a turbine blade is associated with the suction side flow, particular attention is paid to the nature of the unsteady flow on that surface.

Test Facility and Instrumentation

Axial-Flow Turbine

The test facility has been described by, e.g., Hodson.[4] The large scale of the facility (casing diameter 1.524 m) makes it possible to measure the flowfield within the blade passages as well as at exit from and inlet to each blade row.

The inlet to the test facility consists of a large contraction that is fitted with a filter-honeycomb-gauze combination in order to remove the effects of incoming disturbances. This arrangement is followed by a parallel section containing the turbine. Air at atmospheric conditions was drawn through the turbine by a centrifugal fan. The mass flow rate was controlled by throttle vanes situated downstream of the working section.

The working section is shown schematically in Fig. 1. All the instrumentation is computer-controlled, and data are obtained and processed using a dedicated data acquisition system coupled to a microcomputer.

Trip wires (1.2 mm diam) are placed two stator axial chords upstream of stator blades to ensure that the boundary layers at the hub ($\delta^*/h = 0.0060$, $H = 1.41$) and casing ($\delta^*/h = 0.0069$, $H = 1.42$) are turbulent one chord length upstream of the first stator row. Further details of the turbine are given in Table 1.

Blade-Surface Static Pressures

A Scanivalve system with integral pressure transducer is fitted to the rotor. Slip rings transfer power to and signals from the rotor mounted instrumentation. A reference pressure from the stationary frame is provided for the Scanivalve via a single-channel rotating pressure transfer device.

Static pressure tappings, 0.2 mm in diam, are located at 4, 10, 22, 49, 77, 90, and 95% span on the rotor blade. Pressure lines from these tappings are connected to the rotating frame Scanivalve. At each of these radii, a 25-mm-long pitot tube is fitted to the leading edge of a nearby rotor blade. The pressures measured by the pitot tubes provide a reference stagnation pressure at each radius for the determination of the blade surface velocities.

Rotor Flow-Visualization

One of the few surface flow-visualization techniques available for investigations in the rotating frame is that used, e.g., by Joslyn and Dring.[13] This technique relies on the chemical reaction that takes place when ammonia gas comes into con-

Table 1 Turbine geometry and test conditions

|	Stator	Rotor
Flow coefficient, V_{x1}/U_m	0.3	
Stage loading, $\Delta h_0/U_m^2$	1.1	
Stage reaction	0.5	
Midspan stator-rotor gap, mm	47.4	
Hub-tip radius ratio	0.8	0.8
Number of blades	36	42
Mean radius, m	0.686	0.686
Chord, mm	150	124
Axial chord, mm	82.3	63.5
Pitch-chord ratio	0.80	0.83
Aspect ratio	1.01	1.22
Tip clearance, mm	——	1.4
Hub inlet angle, from axial	0.0 deg	37.7 deg
Midspan inlet angle, from axial	0.0 deg	4.5 deg
Tip inlet angle, from axial	0.0 deg	−32.6 deg
Hub exit angle, from axial	74.2 deg	−70.2 deg
Midspan exit angle, from axial	73.7 deg	−72.9 deg
Tip exit angle, from axial	73.2 deg	−75.3 deg
Rotational speed, rpm	——	550
Chord-based Reynolds number	4.7×10^5	3.8×10^5
Inlet freestream turbulence	0.25%	——
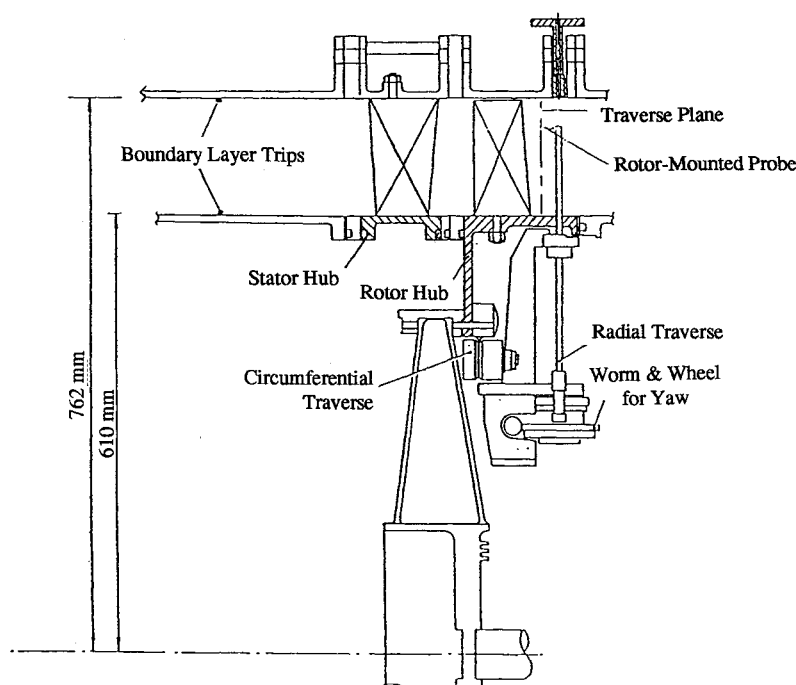
Fig. 1 Large-scale low-speed axial flow research turbine.

tact with diazo paper fixed to the surfaces of the rotor blade. The ammonia gas is ejected through the static pressure tappings in the surface of the blade. The gas was provided via the single-channel rotating pressure transfer device while a rotating-frame Scanivalve was used to direct the gas to the pressure tappings.

The typical exit velocity of the ammonia from a tapping was less than 0.01% of the freestream velocity and, thus, unlikely to affect the main flow. Although ammonia (molecular weight of 17 kg/kmol) is much lighter than air (29 kg/kmol), experiments by other investigators[13,14] have shown that the buoyancy effects are negligible.

Pneumatic Probe Traverses

Traverse mechanisms providing movement in the circumferential, radial, and yaw directions are located downstream of each blade row in the stationary frame. In addition, a three-axis rotating-frame traverse system is provided at exit from the rotor (Fig. 1).

The flow at exit from the stator blades was traversed using a fixed-direction, sting-mounted five-hole probe positioned at 18% axial chord downstream of the stator blades. The probe had a diameter of 2 mm. The five-hole probe was calibrated in an open jet facility using procedures similar to those used for calibrating probes for high-speed flows.[15] Due to wall proximity effects, data were not obtained with the five-hole probe closer than 2 mm to a surface. Near the endwalls, a small pitot tube supplemented the data from the five-hole probe.

A small pitot tube was mounted in the rotating frame traverse system with its axis aligned parallel to the mean flow direction at midspan. Data will be presented from a traverse obtained at 60% axial chord within the rotor passage. This location approximately coincides with where the throat meets the suction surface. Data were not obtained with the probe closer than 1 mm to a surface.

Three-Axis Hot-Wire Anemometer Traverses

The development of the stator flow within the rotor blade passages was investigated using a subminiature, three-axis hot-wire probe. The probe was mounted in the rotating frame traverse system with its axis aligned parallel to the mean flow direction at midspan. Data will be presented from a traverse obtained at 60% axial chord within the rotor passage.

A traverse of the stator exit flow was obtained at 20% axial chord downstream of the stator blades in the stationary frame using the same probe.

The probe had a measurement volume 2 mm in diam. Due to the length-diameter ratio of the hot-wire sensors, it was inappropriate to use the "cosine law" or its modifications[16] to represent the response of the sensors to differing angles of attack. For this reason, a technique similar to that used for calibrating five-hole pneumatic probes was developed. The technique relied on the interpolation of data contained in a lookup table. Two nondimensional coefficients, derived from the apparent velocities indicated by the three sensors, were used as coordinates for the table. Due to wall proximity effects, data were not obtained with the probe closer than 2 mm to any surface.

Each anemometer output signal was recorded at a logging frequency of 50 kHz using a computer-controlled, 12-bit transient-capture system.

Surface-Mounted Hot-Film Anemometers

The development of the suction-side flow on the rotor blades was investigated using spanwise arrays of Dantec 55R47-type surface-mounted constant temperature hot-film anemometers. Nine individual sensors, each 1×0.1 mm in size, were positioned at intervals of 10% span. The sensors were repositioned at different chordwise locations between experiments.

The similarity between the velocity profile adjacent to the wall and the temperature profile of the thermal boundary layer, generated by the heated sensor, leads to a relationship between the rate of heat transfer to the fluid and the wall shear stress of the form[17]

$$\tau_w = k[(E^2 - A^2)/\Delta T]^3 \tag{1}$$

where A and k are constants, ΔT is the temperature difference between the air and the heated sensor, and E is the instantaneous output voltage from the anemometer bridge. In the previous work[4] carried out at low speed, individual hot-film gauges have been calibrated. In the present case the calibration of an array would have been difficult and time-consuming. However, uncalibrated hot-films can provide useful information about the state of the boundary layers. It was therefore decided to adopt a procedure similar to that used previously.[7,14]

A in Eq. (1) is assumed to be approximately equal to the voltage E_0, measured under zero-flow conditions. Additionally, ΔT is proportional to E_0^2. Hence, the approximate expression

$$\tau_w \alpha [(E^2 - E_0^2)/E_0^2]^3 \tag{2}$$

is used to provide values of the wall shear stress, albeit in arbitrary units. In practice, Eq. (2) reduces the effects of the small differences in sensor area, sensor and lead resistance, etc., upon the "calibrations" of the various sensors so that the relative magnitude of the output signals from different sensors can be compared even though the units associated with the quantity τ_w are arbitrary. However, it must be noted that the quantity $(E^2 - E_0^2)$ is of the same order as E_0^2, so that care must be taken when interpreting data in this way.

The upper frequency limit of the sensors, as indicated by "square-wave" tests, was of the order of 30 kHz. The upper frequency limit is such that only the lowest frequencies of the spectra associated with turbulent flow were detected. The blade passing frequency was 330 Hz.

Each anemometer output signal was recorded at a logging frequency of 50 kHz using the transient-capture system. During each experiment, the output signal from each hot film anemometer was acquired as a dc-coupled signal, and then as an amplified, ac-coupled signal (0.01-Hz cutoff). An appropriate anti-aliasing filter was also used. The anemometer output signal was recomposed by adding the mean value determined from the dc-coupled data to the ac-coupled data.

Ensemble-Averaging and Data Presentation

All the measured voltages were converted according to appropriate physical quantities (e.g., shear stress, velocity) before the determination of the statistical quantities.

The acquisition of data was triggered using a once-per-revolution signal. The ensemble-mean of N realizations of a quantity $\alpha(t, n)$ is then defined by

$$\langle \alpha(t) \rangle \equiv \frac{1}{N} \sum_{n=1}^{N} \alpha(t, n) \tag{3}$$

where t is measured from a once-per-cycle datum point for a periodic process. The time-mean of $\alpha(t, n)$ is denoted by $\bar{\alpha}$.

The ensemble rms is defined as

$$\sqrt{\langle\langle \alpha(t)^2 \rangle\rangle} \equiv \sqrt{\frac{1}{N} \sum_{n=1}^{N} [\alpha(t, n) - \langle \alpha(t) \rangle]^2} \tag{4}$$

It represents the amount of deviation, positive or negative, from the average value of the signal at that phase. The time-mean rms value is determined according to

$$\sqrt{\langle\langle \bar{\alpha}^2 \rangle\rangle} \equiv \sqrt{\frac{1}{\tau} \sum_{t=1}^{\tau} \langle\langle \alpha(t)^2 \rangle\rangle} \tag{5}$$

For presentation of the unsteady measurements, t is non-dimensionalized by the wake passing period τ. The surface distance coordinate s has been measured from the geometric leading edge. It is usually expressed as a fraction of the maximum surface distance s_{max}. The spanwise coordinate is usually expressed as a fraction of the distance from the hub.

Results and Discussion

Stator Exit Flow

Figure 2a presents contour plots of the stagnation pressure loss determined from the five-hole probe measurements behind the stator blades. The loss of stagnation pressure associated with the blade wakes extends over much of the span. Near the hub, where the lowest value of stagnation pressure is to be found, there is evidence of secondary flow. At the casing, secondary flow also exists, but the loss core is more diffuse than at the hub. This difference is due to the effects of the spanwise pressure gradients within the stator passage. The centers of these vortices, which are presumed to be coincident with the location of maximum streamwise vorticity, are indicated in Fig. 2a. The passage vortices are centered nearer the relevant end of the blades than the location of maximum stagnation pressure loss. The centers of high loss and streamwise vorticity will tend to move together as the flow develops beyond the traverse plane.

Contours of the mean rms intensity derived from the three-axis hot-wire data are presented in Fig. 2b. The rms of the random velocity fluctuations presented in Fig. 2 and in subsequent figures represents the average of the contributions of all three velocity components. The rms intensity is calculated by dividing the time-mean of the rms by the time-mean midspan stator exit velocity. (The same reference velocity is used to nondimensionalize all of the rms data obtained with the three-axis hot-wire.) It should be recognized that the rms of the velocity fluctuations contains not only information about
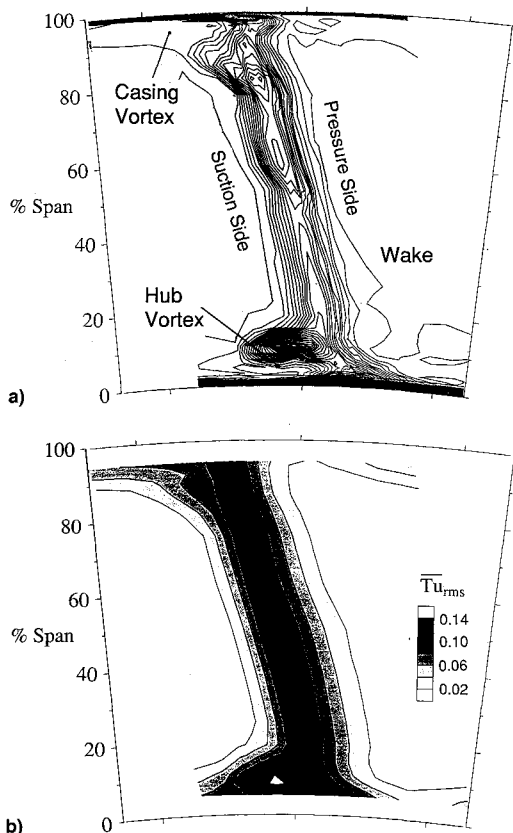
the turbulence in the flow, but also about any fluctuations that are not exactly phase-locked to the rotation of the machine. In the present data, the contribution of the latter is very small since the potential field of the rotor is relatively weak at this location. Indeed, data indicate that the maximum amplitude of the periodic fluctuations of the ensemble-mean velocity are less than 1% of the mean value.

The rms data in Fig. 2b present a very similar picture to that of the stagnation pressure loss data in Fig. 2a. In the center of the wakes, the maximum value of the rms intensity is approximately 9%. In the passage vortex near the casing, the value rises to about 7%. In the passage vortex near the hub, the highest value of almost 15% is reached. Given that stator wakes are known to promote premature laminar-turbulent transition of the suction surface boundary layers, the effects of the secondary flow vortices are expected to be as significant.

Figure 2 has shown that the "two-dimensional" flow occupies a large proportion of the span. This is because there are relatively thin boundary layers at inlet to the blade row and because there is a relatively small amount of turning ($\sim$74 deg) allied to a relatively large velocity ratio ($\sim$3.5) across the blade row. It is also noted that flow-visualization and other data that are not presented indicate that the flow adjacent to the blade surfaces is mainly laminar.

Rotor Surface Flow-Visualization

The results of the rotor suction surface flow-visualization study, obtained at the design condition, are presented in Fig. 3. In the photograph, the line of sight is approximately normal to the midspan chord line. The leading edge cannot be seen.

The results of Fig. 3 show that on the suction surface, the flow at midspan is essentially two dimensional. Here, and elsewhere, the traces of ammonia emitted from the most upstream holes mask the traces of the downstream holes, indicating that there is little or no radial movement of the flow at these spanwise positions.

The flow-visualization also indicates the presence of three-dimensional flows. Near the hub, the effects of the secondary flow are evident. At the trailing edge, the hub secondary flow appears to extend to approximately 30% span. Very near the tip, the presence of the tip leakage vortex is indicated by the traces that extend toward the tip. Just inboard of this region, the effects of secondary flow are apparent. At the trailing edge, the effects of these flows are limited to approximately the outer 25% of span.

Rotor Velocity Distributions

The velocity distributions of the rotor blade, corresponding to five spanwise locations and calculated from the blade surface static pressure data, are shown in Fig. 4. It can be seen that the rotor is moderately forward-loaded with very little

Fig. 2 Stagnation pressure loss and time-mean rms intensity behind the stator blades: a) ω, contour interval 0.02 and b) $\overline{Tu}_{rms}$, contour interval 0.02.
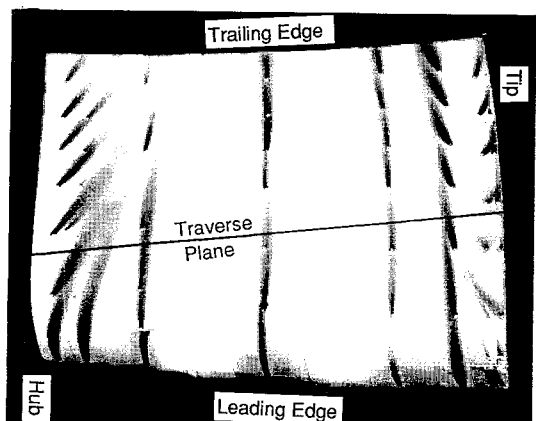

Fig. 3 Results of rotor suction side flow visualization experiment using ammonia-diazo paper.
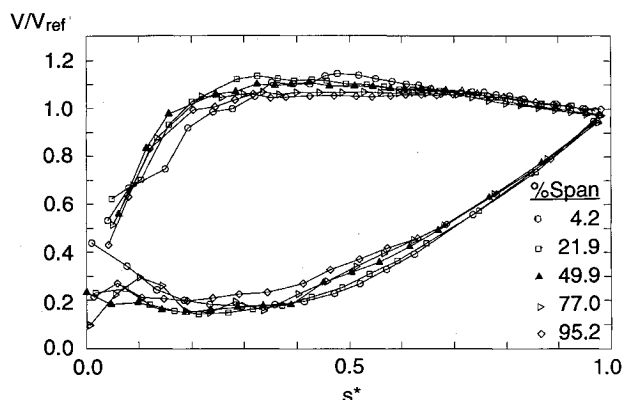
Fig. 4 Rotor blade surface isentropic velocity distributions.

Fig. 5 Relative stagnation pressure loss and minimum ensemble-rms intensity near rotor midchord: a) ω, contour interval 0.05 and b) $\langle\langle Tu_{rms}\rangle\rangle_{min}$, interval 0.005.

deceleration on the suction surface. Peak velocities occur near $0.4s^*$ on the suction surface. At midspan, there is a 14% reduction in velocity from the peak value to the trailing edge of the suction surface. Toward the hub, the diffusion increases slightly. Toward the tip, it reduces. Very close to the hub and the casing, the effects of the secondary and tip leakage flows can be seen in the distortions of the suction side velocity distribution. At each radius, the diffusion is sufficient to cause laminar separation should laminar flow conditions prevail on the back surface of the blade.

The suction side boundary layer will be referred to below. In the case of the pressure surface, it is noted here that the momentum-thickness-based Reynolds number Re_θ predicted by a two-dimensional laminar boundary-layer code does not exceed 130 at any radius. Correlations[18,19] indicate that laminar-turbulent transition is unlikely to occur, irrespective of the freestream conditions. Experimental observations confirm this expectation. In consequence, the pressure surface flow is not discussed further.

Rotor Internal Flow—Steady

The results of traversing the pitot tube and the three-axis hot-wire at 60% axial chord are summarized in Fig. 5.

The data obtained from the rotor-leading-edge pitot tubes have been interpolated to provide a reference stagnation pressure for the traverse data. The velocity data were obtained using the three-axis hot-wire sensor. The intersection with the suction surface, of the traverse planes located within the rotor blade passage, is indicated in the flow-visualization results of Fig. 3.

Figure 5a presents the rotor-relative stagnation pressure losses as measured by the pitot tube. The suction side boundary layer can be seen in the midspan region. In contrast, the pressure side boundary layer is not visible in the figure due to its small size and the restrictions placed on the extent of the traverse by the geometry of the turbine.

Figure 5a shows that at least 50% of the span is occupied by essentially two-dimensional flow. Near the hub, the loss associated with the secondary flow is also evident. At this traverse plane, the low levels of loss away from the suction surface-hub corner region suggest that the passage vortex is relatively weak. Even so, the effects of the secondary flow extend to about 25% of span. The flow-visualization indicates a similar extent for the secondary flow near the hub. The losses associated with the tip leakage vortex are also visible in Fig. 5a. The plot suggests that the tip leakage flow is the dominant secondary flow effect at this location. Traverse data obtained further downstream show a similar result. The vortex appears to be centered near 95% span. The flow-visualization suggests a similar position. The casing secondary flow extends inwards from this region to approximately 75% span. The lower level of stagnation pressure loss associated with this flow suggests that it is relatively weak when compared to the tip-leakage flow.
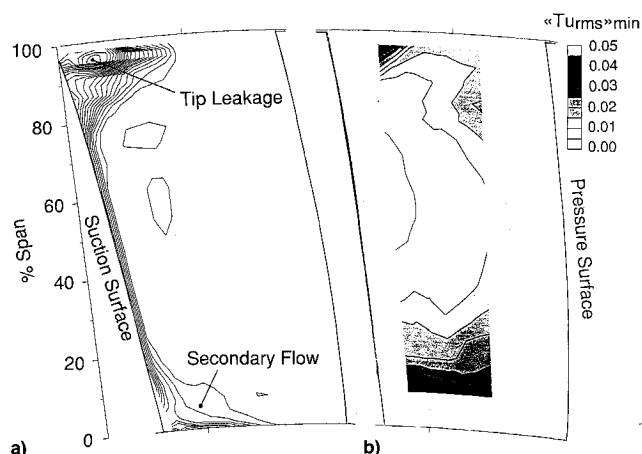
Figure 5b shows the distribution of the minimum level of random unsteadiness within the traverse plane. The minimum value has been selected since examination of the data suggests that the minimum level is the most indicative of the levels that would exist if rotor inflow were undisturbed. The data are again nondimensionalized by the stator midspan time-mean exit velocity, which is almost equal to the rotor relative exit velocity. Due to the size of the probe, the traverse does not cover the same area as the pitot data.

Figure 5b shows that the maximum level of the "undisturbed" rms intensity is approximately 4.5% near 10% span. However, it should be noted that much of the hub secondary flow occurs below this radius. In the tip vortex, the maximum value also reaches 4.5%, but again, much of the detail is absent due to the limits imposed on the size of the traverse plane. In the freestream, away from the effects of the secondary flow and tip leakage flow, the value of the minimum rms intensity is less than 1%, indicating that the stator exit perturbations are separated by regions of low rms intensity as they pass through the rotor blades. Hodson[1] made a similar observation.

Rotor Internal Flow—Unsteady

Figure 6 presents contour maps of the ensemble-rms of the velocity fluctuations at four positions of the rotor blades, equispaced in time over one stator passing period at the same traverse plane as in Fig. 5. To emphasize the unsteady nature of the flow, the minimum level of the ensemble-rms at each traverse point has been subtracted from the ensemble-mean value. Strictly, this is not correct, but much of the unsteadiness occurs in regions of low background random unsteadiness. Therefore, the "error" introduced by this process, which permits the reader to ascertain the true level of $\langle\langle Tu_{rms}\rangle\rangle$ using Figs. 5 and 6, is small. It should also be emphasized that this method of presentation presupposes that the minimum intensity corresponds to the flow that would occur if the rotor inflow were steady.

It is to be expected that the wakes and secondary flow structures will be chopped, sheared, and stretched as they convect through the rotor blade passage.[1] The differing convection rates means that transport of fluid that lies near the suction surface is much more rapid than of that which lies close to the pressure surface. Since the traverse plane is located near midchord, most of the distortion will have already taken place. In consequence, the stator wakes and secondary flow features are expected to appear first at the traverse plane nearer the suction side of passage. The data presented in Fig. 6 show that this is indeed the case.

Figure 6a shows that the midspan area of the suction surface is exposed to a low level of freestream random unsteadiness
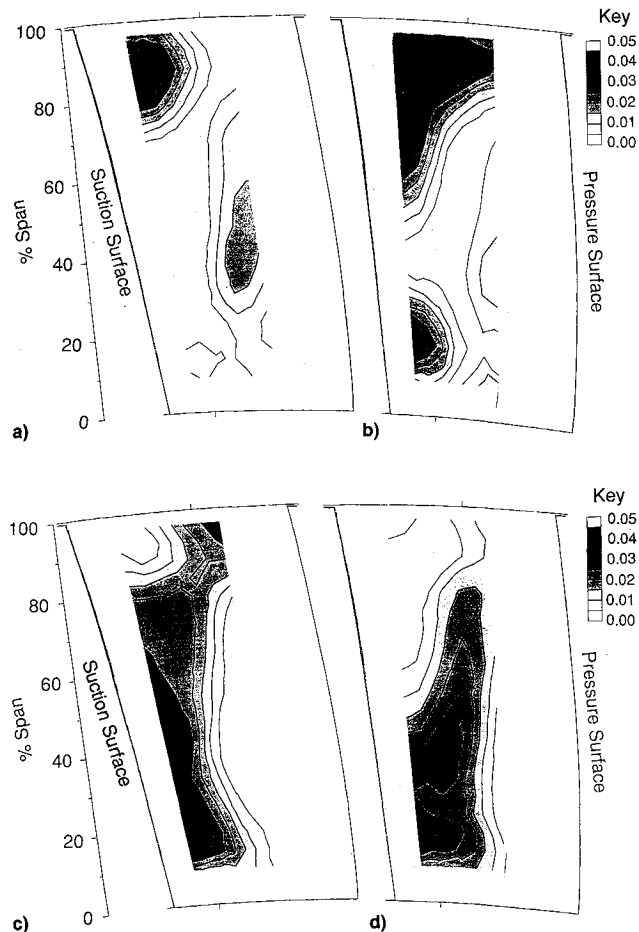
Fig. 6 Instantaneous $\langle\langle Tu_{rms}\rangle\rangle - \langle\langle Tu_{rms}\rangle\rangle_{min}$ near rotor midchord; contour interval 0.005: $t/\tau =$ a) $\frac{1}{8}$, b) $\frac{3}{8}$, c) $\frac{5}{8}$, and d) $\frac{7}{8}$.

at the first rotor position. In contrast, the remnants of a previous wake can be seen toward the pressure side of the passage near midspan. Near the casing, the viscous flow originating from near the casing in the stator row is beginning to appear. It is located at about 85% span close to the suction surface. The contours indicate a peak intensity of approximately 4.5%. This is less than in the stator exit flow. It is presumed that, at this traverse plane, the stator secondary flow and loss regions are coincident. Whatever the case, this feature of the stator exit flow lies inboard of the region occupied by the rotor tip-leakage flow. It is also slightly inboard of the center of streamwise vorticity indicated by the stator exit traverses. Smoke visualization experiments and computational simulations that trace particles through a flowfield produced by a Navier-Stokes code suggest that the inward movement is due to the combined effects of blockage and convection associated with the tip leakage vortex. These flows push the stator secondary flow toward rotor midspan.

Figure 6b occurs one-quarter of a stator passing period after Fig. 6a. The suction surface is now exposed to an incoming wake. The plot indicates that the contours reach a maximum value of approximately 4.5% in the stator wake. (The velocity on the suction surface is approximately equal to the reference velocity; see Fig. 4.) This value is lower than at stator exit, which indicates that there has been a decrease in the turbulent kinetic energy of the wakes downstream of the stator traverse plane. On the pressure side of the passage, Fig. 6a shows that the level of the random unsteadiness is lower still. This difference suggests that the stretching of the wake may be partly responsible for this reduction in random unsteadiness since this occurs more toward the pressure side. Although the level of the random unsteadiness is lower on the pressure side of the passage, the velocity is also lower. As a consequence, the

turbulence intensity near to the pressure surface, is as high as on the suction side.

Figure 6b also indicates that the feature that is believed to represent the stator casing secondary flow has moved toward the pressure surface. The appearance on the pressure side at this later time is a consequence of the convection processes as described above. It is also located slightly nearer casing. This is believed to be because the effects of the tip-leakage vortex are reduced away from the suction side.

Besides the wake and stator casing secondary flow, a feature that is identified with the stator hub secondary flow is also visible in Fig. 6b. It is centered at approximately 20% span near the suction side of the passage. This is at a larger radius than the location indicated by the stator exit traverses. Following the visualization experiments using smoke and the use of CFD predictions, it is believed that this radial shift is due to the effects of blockage and convection associated with the rotor secondary flows. The maximum value indicated by the contours associated with this phenomenon is approximately 4.5%. This is considerably less than the maximum value measured at exit from the stator row.

At one-quarter of a stator passing period after Fig. 6b, Fig. 6c shows that the wake now extends from near the pressure side at the larger radii to the suction side near the inner radii. The stator casing secondary flow is just apparent in the plot, whereas the hub secondary flow remains visible. The skewed nature of the wake and the locations of the stator secondary flow features are consistent with the convective processes described above. The final plot in Fig. 6 shows that the stator hub secondary flow has moved further toward the pressure surface.

In the case of the stator secondary flows, the plots of Fig. 6 have shown that significant dissipation occurred between the midchord traverse plane and the stator exit traverse plane. Typical maximum levels of the random freestream disturbances are of the order of 4–5%. Given that the secondary flow vortices emanating from the stator blades are being stretched so that their associated kinetic energy rises, the similarity inside the rotor passage between the disturbance levels in the wakes and secondary flow regions might not be expected. This is especially so in the case of the hub secondary flow.

For the sake of brevity, data from only one traverse plane have been presented here. However, the nature of the flow is similar at other chordwise locations. In particular, the stator secondary flow features continue to appear inboard of the rotor secondary and tip leakage flows when they are close to the suction surface. An analysis of the exit vorticity of the stator and rotor blade rows reveals that the secondary flows are much stronger in the rotor. Because of the relative strengths of the secondary flows, the effects of the stator exit flowfields on the rotor secondary flows appear to be small. It is believed that this explains why Figs. 5 and 6 have suggested that the three-dimensional unsteady flow inside the rotor passages is convected by the rotor secondary and tip-leakage flows. This is an important observation since the appearance of the stator secondary flow features inboard of the rotor secondary flows influences the development of the rotor suction side boundary layers. By affecting the nature of laminar-turbulent transition as discussed in the next section, the rotor profile loss is undoubtedly increased. Should the vortices have burst, a different result may have emerged.

Suction Surface Unsteady Flow

Wake-induced and steady flow bypass transition begin with the formation of turbulent spots. The formation and growth of these spots may be studied using surface-mounted hot-film anemometers.[6] Before examining the impact of the stator secondary flows on the whole of the rotor suction surface, a brief description of the development of the rotor midspan

boundary layer will be presented. At midspan, the transition process is initiated by the stator wakes.

Figure 7 presents a selection of the raw hot-film traces obtained at midspan. Ten wake-passing cycles are shown for each gauge. It should be noted that the output from each gauge was not acquired during the same revolution of the rotor. As a consequence, it is not possible to trace the development of specific events from one gauge to the next. Nevertheless, it is possible to ascertain that wake-induced transition has begun before $0.3s^*$. By $0.4s^*$, wake-induced transition is clearly evident. For example, transient regions of relatively high wall shear stress associated with turbulent flow can be seen near $t^* = 4$ and $t^* = 5$. Further data obtained in this turbine suggest that transition begins near $0.16s^*$,[6] where Re_{θ} is approximately 150.

An important result can be obtained by examination of the raw traces in Fig. 7. Each wake-passing event is associated with the formation of zero, one, two or perhaps more turbulent spots. The formation is therefore not completely phase-locked to the wake-passing. Instead, the presence of the wake must be viewed as providing a region of flow that is susceptible to the formation of turbulent flow. This confirms the results of previous investigations.[20] It seems that the formation of turbulent spots under the influence of the wakes is a stochastic process similar to that which occurs in steady flow bypass transition.

Over the rear part of the midspan suction surface, e.g., at $0.8s^*$, the turbulent events occur each time a wake passes the sensor in question. These events also occupy a greater proportion of the stator-passing cycle. However, distinct periods of laminar flow are also evident. The increased duration of the turbulent events arises because as the turbulent spots move downstream, their leading and trailing edges have propagation rates approximately equal to 0.9 and 0.5 of the freestream velocity, as would be expected from steady flow experiments.[6] As the spots become elongated, they reside over

Fig. 7   Midspan wall shear stress $\tau_w(t)$ traces derived from surface-mounted hot-film data.

the sensors for a greater proportion of the time. The occurrence of a turbulent event each time a wake passes arises because as the turbulent spots move downstream, their spanwise extent increases. Therefore, just as in steady flow transition, turbulent spots formed at spanwise locations adjacent to midspan will eventually be detected by the sensors at midspan. By the trailing edge, the output traces indicate that the boundary layer is almost fully turbulent as a result of the chordwise and spanwise growth of the turbulent spots.

Since the formation of turbulent spots under the influence of the wakes is a stochastic process similar to that which occurs in steady flow bypass transition, the ensemble-averaged data will be used to describe the impact of the unsteady flow on the remainder of the suction surface.

Figure 8 presents a distance-time diagram of the ensemble-mean shear stress at several spanwise locations. Three wake-passing intervals are shown in each plot. The contours denote the difference between the ensemble-mean $\langle \tau_w \rangle$ and its minimum value at the same location. This form of presentation emphasizes the periodic fluctuations, at the expense of providing an indication of the changes in the mean level. This is because the change in wall shear stress that accompanies the change from laminar to turbulent flow is approximately constant, even though the actual levels vary. This form of presentation is particularly suitable for situations where laminar flow exists at some part of the periodic cycle. When the flow approaches the fully turbulent condition, the amplitude of the ensemble-mean wall shear stress reduces.

Trajectories corresponding to the freestream velocity U_x, and one-half of the freestream velocity $0.5U_x$ are shown in Fig. 8. The wake is expected to convect at approximately the freestream velocity. The rear of a turbulent spot is expected to travel at about one-half of the freestream velocity. The front is expected to propagate at about $0.9U_x$.

Figure 7 has presented the raw data that were obtained at 50% span. Figure 8 contains the distance-time diagram for the same set of data. By $0.4s^*$, transition was clearly visible in the raw data presented in Fig. 7. Figure 8 shows that at this location, a triangular region of relatively high wall shear stress begins to emerge. The leading edge of this region propagates with a velocity that is similar to that of the freestream, whereas the rear propagates at about one-half of that value. This type of behavior is consistent with the development of wake-induced transition.[6] By the trailing edge, at midspan, Fig. 8 shows that the wake-induced regions of flow created by consecutive wakes have almost merged to form a continuously turbulent boundary layer. It is not the intention here to discuss in detail the development of the unsteady suction-side transitional flow.[6] However, it seems that attached laminar flow persists in between the wake passing events beyond the point at which a steady laminar boundary layer would separate and undergo transition. This is believed to be because a period of time is required after the end of turbulent flow before "steady" laminar flow can be re-established.

Figure 8 reveals that the behavior of the flow between 40–60% span is similar to that at midspan. Periodic transition seems to begin at approximately the same surface distance and at about the same time during each cycle. Transition appears to be almost complete by the trailing edge in each case. Given the resemblance of the velocity distributions (Fig. 4) and the uniformity of the stator wake (Fig. 2) over this part of the span, the similarities noted in Fig. 8 suggest that the stator wakes are responsible for the observed mode of transition between 40–60% span.

Figure 8 also indicates that periodic transition occurs at 70% span. The form of the diagram is very similar to that which occurs between 40–60% span. However, at 70% span, transition begins nearer the leading edge. Since the velocity distributions (Fig. 4) are very similar over this part of the blade surface, it is suggested that a more intense disturbance is responsible for this difference. Figure 8 also shows that at
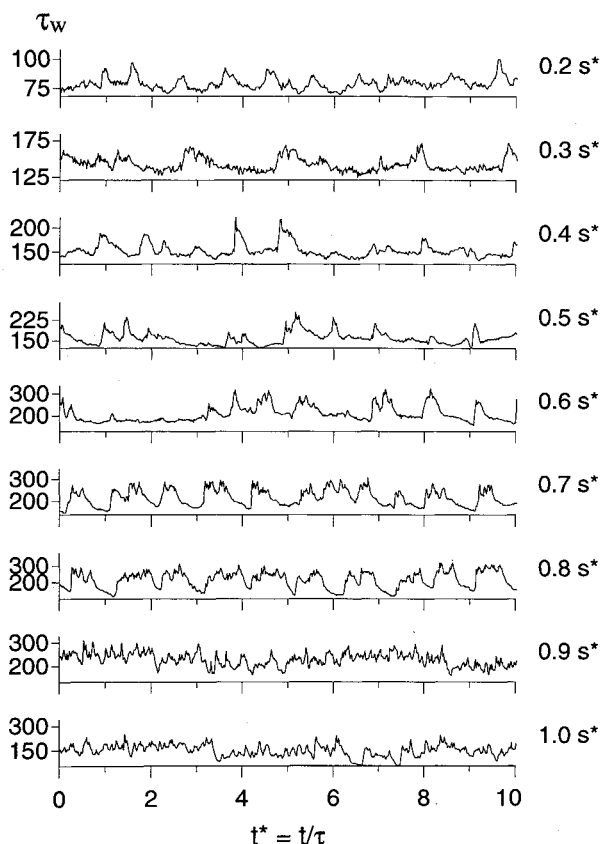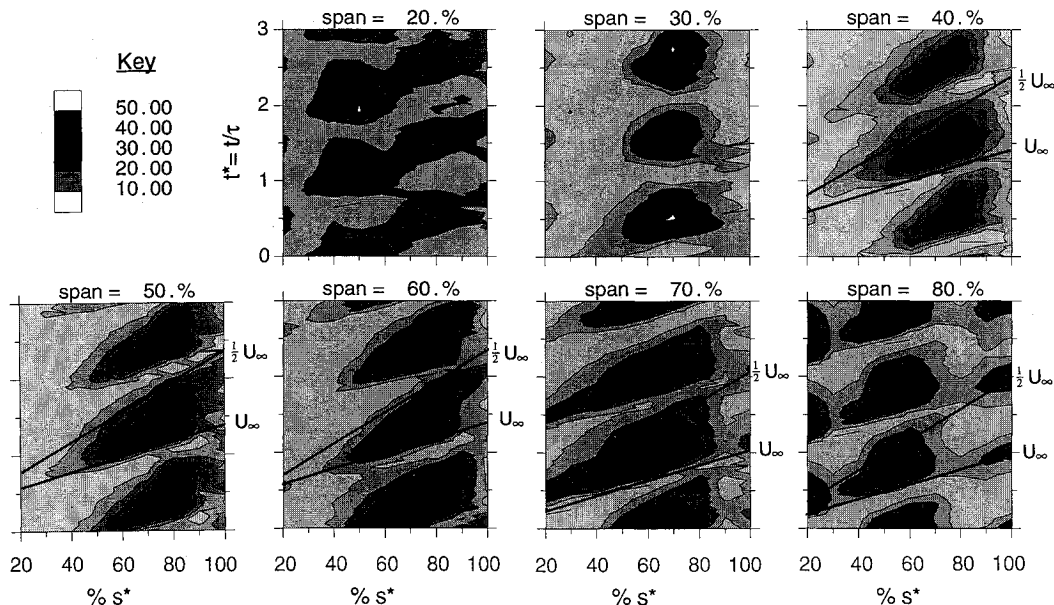
Fig. 8 Distance time-diagram of ensemble-mean wall shear stress expressed as the deviation from minimum value at the same surface location, i.e., $\langle \tau_w(s, z, t) \rangle - \langle \tau_w(s, z) \rangle_{min}$.

70% span, the disturbance arrives at an earlier time at the first sensor. The two differences that have just been noted suggest that the phenomenon responsible for transition at 70% span might be the stator casing secondary flow. Figure 6 shows that this arrives earlier than the wake. At 80% span, Fig. 8 reveals that the transition process is initially similar to that which occurs at 70% span, but that the length of the transition zone appears to be truncated. This is believed to be because the secondary flows extend from the tip to cover these sensors at about $0.7s^*$ (Fig. 3).

At 30% span, the raw data traces revealed that periodic transition had only just begun by $0.5s^*$. By $0.7s^*$, a turbulent flow existed almost continuously. Figure 8 shows that significant periodic variations exist only between $0.5-0.7s^*$ at this spanwise location. At 20% span, the raw data and distance-time diagram (Fig. 8) exhibit a very similar pattern, with the exception that the sensor that provides the primary evidence of unsteady transition is located at $0.5s^*$. The reasons for these observations are not fully understood, but are believed to be associated with the arrival of the stator hub secondary flow vortex, and the proximity of the rotor hub secondary flow region.

The distance-time diagrams corresponding to 10 and 90% span have not been presented here. This is because the secondary and tip-leakage flows dominate these areas of the blade suction surface. Since the data from these sensors contain very little evidence of periodic flow, it is suggested that the near-surface flow associated with these phenomena is not significantly affected by periodic phenomena. The raw signals produced by the hot-film sensors indicate that, in both cases, the flow is either predominantly or entirely turbulent in these regions.

Figure 9 presents a different view of the data shown in Fig. 8. It shows the distribution of the ensemble-mean wall shear stress as the rotor blade changes circumferential position. Data from four equispaced intervals are shown. The time-sequence is the same as that shown elsewhere. Although the measurement grid consists of only 9 by 9 surface locations, the salient features of the flow may be identified. The extent of the rotor secondary flow, as indicated by the surface flow-visualization, is also shown.

The sequence of contour maps in Fig. 9 shows that at no time does the effect of the wakes extend to the hub or the casing. This is due to the action of the rotor secondary flows. The effect of the wakes on the boundary layers near midspan
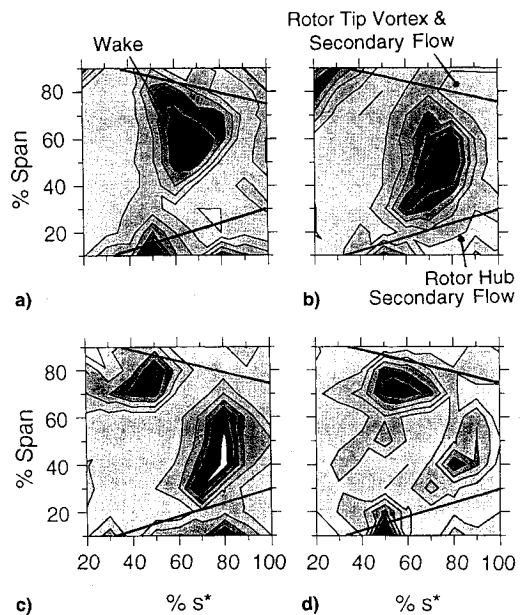

Fig. 9 Instantaneous of ensemble-mean wall shear stress expressed as the deviation from minimum value at same surface location, i.e., $\langle \tau_w(s, z, t) \rangle - \langle \tau_w(s, z) \rangle_{min}$; for key, see Fig. 8: $t/\tau =$ a) $\frac{1}{8}$, b) $\frac{3}{8}$, c) $\frac{5}{8}$, and d) $\frac{7}{8}$.

can be seen. Due to the nature of the convection processes inside the rotor passage, the wakes lie further along the surface nearer the tip and closer to the leading edge at smaller radii. Figure 9 shows that, as might be expected, the leading edge of the wake-induced transition zone exhibits a similar form. In Fig. 9d, the effects of two consecutive wakes may be seen.

In Fig. 9c, the region of high-valued contours near the tip indicates the effect of the stator casing (secondary) flow referred to in the discussion of Fig. 8. This feature is associated with the wake that follows that which is visible in Fig. 9b. The sequence of figures from Figs. 9b–9d suggests that the effect of this flow, and perhaps the secondary flow itself, convect along a path parallel to the line that indicates the extent of the rotor tip-leakage flow. Presumably, the relative strengths of the stator and rotor three-dimensional flows are responsible for this observation. Since the passage vortices of

an upstream blade row are usually more significant than the wakes, the convection of these vortices through the next blade row is more likely to be responsible for the unsteady transitional flow that arises nearer the ends of the blades. Since the effect of the three-dimensional flowfield within the rotor passage is to force the effects of these vortices toward midspan when they are adjacent to the suction surface, it would seem that the extent of wake-induced transition is limited to a smaller part of the span than the stator exit flowfield and rotor surface flow patterns would suggest.

The traverses at exit from the stator row (Fig. 2) have indicated that the stator hub secondary flow is more intense than at the casing. Yet, unlike the effects of its counterpart at the casing, the effects of the stator hub secondary flow are not particularly evident. Figure 9d reveals what might be the location of the effect of this secondary flow on the suction side flow. It is probable that this difference between the behavior of the flow in the two regions arises because at the hub, the secondary flow tends to lift the flow away from the suction surface, whereas near the tip, the tip leakage flow dominates the flowfield.

Figure 9 shows that the regions near the hub and tip of the rotor suction surface that are dominated by three-dimensional flows contain relatively little evidence of unsteady behavior. This is presumably due to the relative strengths of the stator and rotor three-dimensional flows. It is suggested that the stator secondary flows do not have a significant effect on the loss generation processes associated with these flows, since much of the loss is produced at the surfaces. If this is generally so, then steady flow calculation methods may be adequate for the prediction of secondary flows and losses in the rotors of axial turbines.

Conclusions

The development of the steady and unsteady three-dimensional flow within the rotor passage of a single-stage axial turbine has been described.

Within the rotor blade passage at about 60% axial chord, the stator wakes are separated by regions of low-turbulence intensity as they pass through the rotor blades. A maximum value of approximately 4% is reached in the stator wake at the same plane, which is less than that by the stator exit traverse. In the case of the stator secondary flows, significant dissipation seems to have occurred between the traverse planes, so that the maximum levels of the random disturbances are of a similar magnitude to those in the wake.

Due to differences in the relative strengths of the secondary flows, the effects of the stator secondary flows on the rotor secondary flows appear to be small. The effect of the three-dimensional flowfield within the rotor passage is to force the effects of these flow features toward midspan. As a consequence, it would seem that the extent of wake-induced transition is limited to a smaller part of the span than the stator exit flowfield and rotor surface flow patterns would suggest.

Acknowledgments

References

[1]Hodson, H. P., "Measurements of Wake-Generated Unsteadiness in the Rotor Passages of Axial Flow Turbines," *Journal of Engineering for Gas Turbines and Power*, Vol. 107, April 1985, pp. 467–476.

[2]Sharma, O. P., Renaud, E., Butler, T. L., Milsaps, K., Dring, R. P., and Joslyn, H. D., "Rotor-Stator Interaction in Multi-Stage Axial-Flow Turbines," AIAA Paper 88-3013, July 1988.

[3]Yamamoto, A., Mimura, F., Tominaga, J., Tomihisa, S., Outa, E., and Matsuki, M., "Unsteady Three-Dimensional Flow Behaviour Due to Rotor-Stator Interaction in an Axial Flow Turbine," American Society of Mechanical Engineers Paper 93-GT-404, June 1993.

[4]Hodson, H. P., "Boundary Layer and Loss Measurements on the Rotor of an Axial Flow Turbine," *Journal of Engineering for Gas Turbines and Power*, Vol. 106, April 1984, pp. 391–399.

[5]Doorly, D. J., and Oldfield, M. L. G., "Simulation of the Effects of Shock Wave Passing on a Turbine Rotor Blade," American Society of Mechanical Engineers Paper 85-GT-112, June 1985.

[6]Hodson, H. P., Addison, J. S., and Shepherdson, C. A., "Models for Unsteady Wake-Induced Transition in Axial Turbomachines," *Journal de Physique et le Radium*, Vol. 2, No. 4, 1992, pp. 545–574.

[7]Hodson, H. P., Huntsman, I., and Steele, A. B., "An Investigation of Boundary Layer Development in a Multistage LP Turbine," American Society of Mechanical Engineers Paper 93-GT-310, June 1993.

[8]Binder, A., "Turbulence Production Due to Secondary Vortex Cutting in a Turbine Rotor," *Journal of Engineering for Gas Turbines and Power*, Vol. 107, Oct. 1985, pp. 1039–1046.

[9]Sharma, O. P., Pickett, G. F., and Ni, R. H., "Assessment of Unsteady Flows in Turbines," American Society of Mechanical Engineers Paper 90-GT-150, June 1990.

[10]Binder, A., Förster, W., Mach, K., and Rogge, H., "Unsteady Flow Interaction Caused by Stator Secondary Vortices in a Turbine Rotor," American Society of Mechanical Engineers Paper 86-GT-302, June 1986.

[11]Arndt, N., "Blade Row Interaction in a Multistage Low-Pressure Turbine," American Society of Mechanical Engineers Paper 91-GT-283, June 1991.

[12]Joslyn, H. D., Dring, R. P., and Sharma, O. P., "Unsteady Three-Dimensional Turbine Aerodynamics," American Society of Mechanical Engineers Paper 82-GT-161, March 1982.

[13]Joslyn, H. D., and Dring, R. P., "Turbine Rotor Negative Incidence Stall," American Society of Mechanical Engineers Paper 83-GT-23, March 1983.

[14]Hodson, H. P., and Addison, J. S., "Wake-Boundary Layer Interactions in an Axial-Flow Turbine at Off-Design Conditions," *Journal of Turbomachinery*, Vol. 111, No. 2, 1989, pp. 181–192.

[15]Dominy, R. G., and Hodson, H. P., "An Investigation of Factors Influencing the Calibration of 5-Hole Cone and Pyramid Probes," *Journal of Turbomachinery*, Vol. 115, July 1993, pp. 513–519.

[16]Champagne, F. H., Schleicher, C. A., and Wehrmann, O. H., *Journal of Fluid Mechanics*, Vol. 28, No. 153, 1967, pp. 153–175.

[17]Bellhouse, B. J., and Schultz, D. L., "The Measurement of Fluctuating Skin Friction in Air with Heated Thin-Film Gauges," *Journal of Fluid Mechanics*, Vol. 32, No. 4, 1968, pp. 675–680.

[18]Abu-Ghannam, B. J., and Shaw, R., "Natural Transition of Boundary Layers—the Effects of Turbulence, Pressure Gradient and Flow History," *Journal of Mechanical Engineering Science*, Vol. 22, No. 5, 1980, pp. 213–228.

[19]Mayle, R. E., "The Role of Laminar-Turbulent Transition in Gas Turbine Engines," American Society of Mechanical Engineers Paper 91-GT-261, June 1991.

[20]Addison, J. S., and Hodson, H. P., "Modelling of Unsteady Transitional Boundary Layers," *Journal of Turbomachinery*, Vol. 114, No. 3, 1992, pp. 580–589.